Enhancing the Li Storage Capacity and Initial Coulombic Efficiency for Porous Carbons by Sulfur Doping

Guoqing Ning,*,[†,§] Xinlong Ma,[†,§] Xiao Zhu,[†] Yanming Cao,[†] Yuzhen Sun,[†] Chuanlei Qi,[†] Zhuangjun Fan,[‡] Yongfeng Li,[†] Xin Zhang,[†] Xingying Lan,[†] and Jinsen Gao[†]

[†]State Key Laboratory of Heavy Oil Processing, China University of Petroleum, Beijing 102249, China

[‡]Key Laboratory of Superlight Materials and Surface Technology, Ministry of Education, School of Materials Science and Chemical Engineering, Harbin Engineering University, Harbin, Heilongjiang 150001, China

Ⓢ *Supporting Information*

ABSTRACT: Here, we report a new approach to synthesizing S-doped porous carbons and achieving both a high capacity and a high Coulombic efficiency in the first cycle for carbon nanostructures as anodes for Li ion batteries. S-doped porous carbons (S-PCs) were synthesized by carbonization of pitch using magnesium sulfate whiskers as both templates and S source, and a S doping up to 10.1 atom % (corresponding to 22.5 wt %) was obtained via a S doping reaction. Removal of functional groups or highly active C atoms during the S doping has led to formation of much thinner solid-electrolyte interface layer and hence significantly enhanced the Coulombic efficiency in the first cycle from 39.6% (for the undoped porous carbon) to 81.0%. The Li storage capacity of the S-PCs is up to 1781 mA h g^{-1} at the current density of 50 mA g^{-1}, more than doubling that of the undoped porous carbon. Due to the enhanced conductivity, the hierarchically porous structure and the excellent stability, the S-PC anodes exhibit excellent rate capability and reliable cycling stability. Our results indicate that S doping can efficiently promote the Li storage capacity and reduce the irreversible Li combination for carbon nanostructures.

KEYWORDS: sulfur doping, carbon nanostructure, synthesis, Coulombic efficiency, anode, Li ion battery
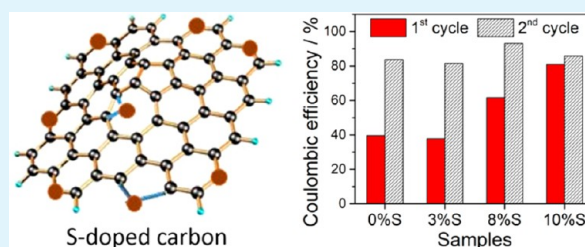
1. INTRODUCTION

Graphite materials have been widely used as reliable low cost anode materials for Li ion batteries (LIBs), with the theoretical capacity of 372 mA h g^{-1} and excellent cycling stability. However, the limited Li storage capacity of the graphite materials falls short of satisfying needs for high power and/or capacity for applications such as power tools and electric vehicles. Reforming the carbon materials by fabricating nanostructures[1−8] (e.g., few-layered graphene and hierarchically porous carbons) or heteroatom doping[9−13] (e.g., N and/or S doping) is an important approach to promote Li storage capacity and maintain excellent cycling stability at the same time. The surface or pore storage of Li ions in carbon nanomaterials leads to higher capacity. The mesopores in the carbon nanostructures are able to reduced diffusion length of Li ions, thus resulting in better rate capability.[14,15] Similarly, heteroatom doped carbons contain more defects through which Li ions can perpendicularly diffuse from outside to inside graphite layers, thus providing more storage regions.[12] However, the carbon nanomaterials used in LIBs usually suffer from large irreversible capacity due to formation of a solid electrolyte interface (SEI) layer on their large surfaces.[2,5,16−18] Therefore, the carbon nanostructures deliver high capacity but low Coulombic efficiency (30%−50%),[5,15] which hinders their actual application as anodes for LIBs due to the high cost. To obtain high Li storage capacity and eliminate the irreversible capacity at the same time still remains great challenge for carbon nanostructures.

Although the prelithiation treatment is capable of reducing the irreversible Li capacity for carbon nanomaterials,[19] in fact, the irreversible consume of Li still occurred in the prelithiation. In our previous work,[20] combination of cobalt species with the defective sites of porous graphene is found to be able to significantly eliminate the irreversible Li combination on the graphene surface. It triggers us to enhance the Coulombic efficiency for carbon nanostructures by treating the highly defective carbon segments that may irreversibly bind Li ions. Here, for the first time, we present a novel strategy to obtain both high Li storage capacity and much enhanced Coulombic efficiency for porous carbons by S doping. S-doped porous carbons (S-PCs) were synthesized by carbonization of pitch using basic magnesium sulfate (BMS) whiskers as both templates and S source. The S-doping up to 10.1 atom % and the well-developed porous structures in the as-prepared S-PCs have led to significantly promoted Li storage capacity and high rate capability as compared to the undoped porous carbon.
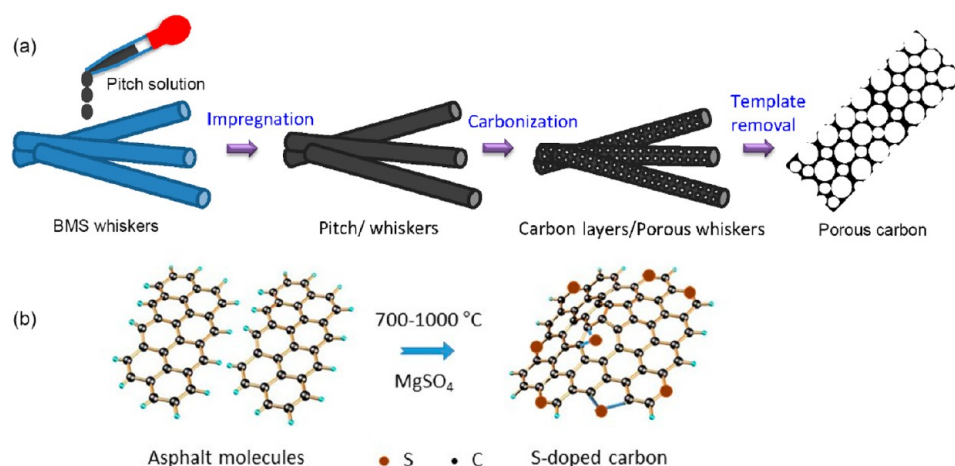
Figure 1. Synthesis process and mechanism of S-PCs. (a) Illustration showing the synthesis process of the porous carbons. (b) S doping reaction that leads to S doping of carbon materials.
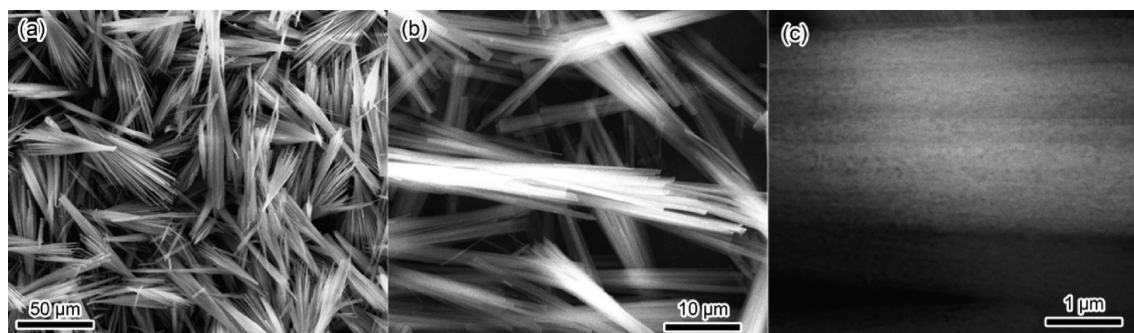

Figure 2. Morphology of the BMS whiskers. SEM images of BMS whiskers before (a) and after a 700 °C calcination (b and c).

Thinner SEI films and much enhanced Coulombic efficiencies are obtained because the S doping reaction has removed the active carbon segments that tend to irreversibly combine with Li ions. Our work demonstrates a reliable new strategy, by S doping, to promote the electrochemical performance of anodes for LIBs.

2. EXPERIMENTAL METHODS

Synthesis of S-PCs. BMS ($5Mg(OH)_2 \cdot MgSO_4 \cdot 3H_2O$) whiskers were prepared by a previously reported hydrothermal process.[21,22] In a typical run, first, ~1 g pitch was dissolved in 30 mL toluene. Then, 10 g BMS whiskers were added into the pitch solution with violent agitation, followed by filtration and drying in an oven at 80 °C. The as-obtained pitch/BMS whisker mixture was set in an alumina boat. The boat was set in a quartz tube reactor, heated in an Ar flow to 700−1000 °C at a rate of 10 °C/min, and calcined for 30 min. After being cooled to room temperature, the obtained black powder was taken out and purified by a hydrochloric acid washing. After an oven drying, a fine powder was obtained as the final product. Synthesis processes with different calcination temperatures (700, 900, and 1000 °C) were performed, and the products were labeled as C700, C900, and C1000, respectively. The none-doped porous carbon (labeled as G1) was prepared using MgO porous whiskers as templates, which were obtained by calcination of the BMS whiskers at 1100 °C.

Characterization. The as-prepared samples were characterized by transmission electron microscopy (TEM, JEM 2010), scanning electron microscopy (SEM, Quanta 200F), scanning transmission electron microscopy (STEM, FEI F20) equipped with energy dispersive spectroscopy (EDS), Raman spectroscopy (Renishaw RM2000, 633 nm), X-ray photoelectron spectroscopy (XPS, PHI700), X-ray diffraction (XRD, D8 ADVANCE), thermogravimetry (TG) analysis (Q500, in air flow with a temperature scan of 10 °C/

min) and nitrogen physisorption (Micrometritics ASAP 2010). The I−V curves were obtained at the CHI660C type electrochemical working station using the compressed pellets (50 mg) of 13 mm in diameter, composed of the as-prepared porous carbons, which were processed in a stainless steel mold by using 10 MPa pressure. The purity of the as-prepared carbon materials was analyzed by an inductively coupled plasma−atomic emission spectrometry (ICP-AES, Varian Vista MPX) with a resolution <0.004 nm and a detection limit in ppb-ppm grade. In the digesting process of the ICP-AES analysis, ~0.25 g carbon material was loaded in a ceramic crucible and calcined in an oven in air up to 700 °C. Then, the obtained ash was dissolved in aqua regia ($HCl/HNO_3 = 3:1$), and no insoluble residue was left. Finally, the solution was diluted by deionized water in a volumetric flask, and the diluted solution was pumped into the ICP-AES apparatus for the analysis. Elementary analysis was carried out using a Vario MICRO Cube CHNS analyzer.

Electrochemical Test. Coin cells were assembled using Li sheets as both reference and counter electrodes. In order to remove any possible solvent or moisture, calcination at 400 °C for 1 h in Ar flow was performed on the carbon materials before assembling the coin-type cells. A slurry containing 70 wt % carbon materials, 10 wt % acetylene black (Super-P) and 20 wt % polyvinylidene fluoride was coated on copper foils to prepare the working electrodes, following by a 105 °C oven drying overnight. One M $LiPF_6$ solution in a 1:1 (volume) mixture of ethylene carbonate (EC) and dimethyl carbonate (DMC) was used as electrolyte. The cells were galvanostatically charged and discharged in the voltage range from 0.01 to 3 V vs Li/Li$^+$ at different current densities. The AC impendence spectra were obtained by applying a sine wave with amplitude of 5.0 mV over the frequency range from 100 kHz to 0.01 Hz.
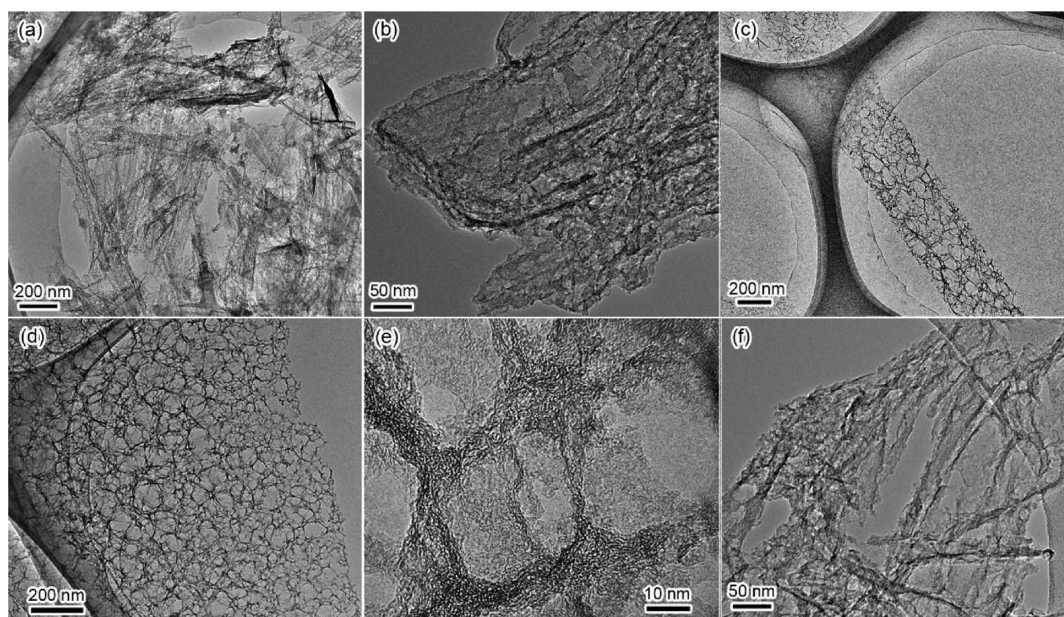
Figure 3. Morphology of the as-prepared porous carbons. TEM images of the porous carbons prepared with calcinations at 700 (a and b), 900 (c–e), and 1000 °C (f).
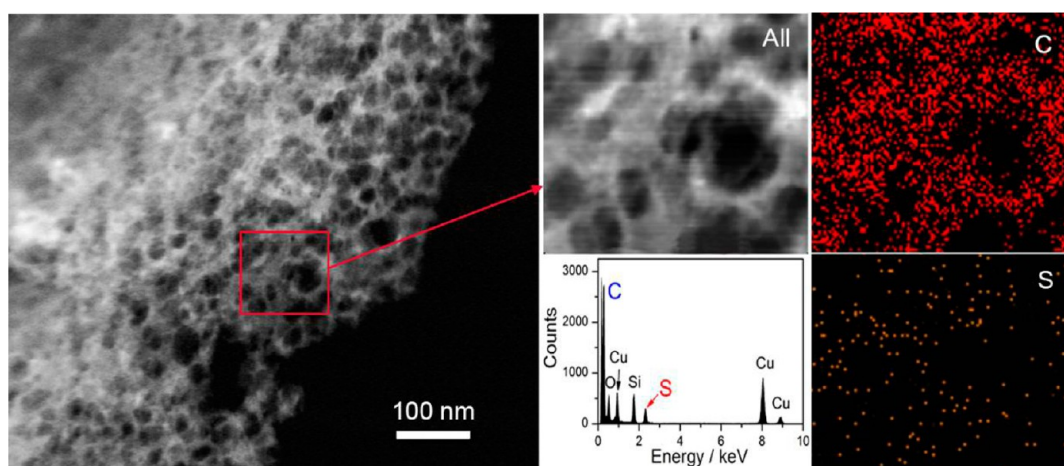

Figure 4. STEM image (left) and EDS mapping (right) of C900.

3. RESULTS AND DISCUSSION

The strategy for the synthesis of S-doped porous carbons is illustrated in Figure 1a. S-doping is achieved during the calcination following the reaction between asphalt and $MgSO_4$, as we call the "S-doping reaction" (Figure 1b). In the S-doping reaction, carbonized pitch reduces $MgSO_4$, while the $MgSO_4$ oxidizes the carbon.[23] The S-PC with a well-controlled porous structure is finally obtained after removal of the template by an acid washing.

BMS ($5Mg(OH)_2 \cdot MgSO_4 \cdot 3H_2O$) whiskers were prepared by a previously reported hydrothermal process.[21,22] As shown in Figure 2a, the as-prepared whiskers have a length ∼100 μm and a diameter ∼2 μm with a smooth surface. TG analysis shows that BMS whiskers decompose at 100−500 °C due to the release of crystal water and the decomposition of $Mg(OH)_2$ (Figure S1 in Supporting Information). As shown in Figure 2b and c, the surface of the calcined whiskers is not smooth, and some pores can be observed. Therefore, the calcined whiskers are porous cylindrical templates. We have measured the specific

surface areas (SSAs) of the whiskers before and after a 700 °C calcination. The SSA and pore volume of the calcined whiskers are 10.0 m^2/g and 0.05 cm^3/g, slightly higher than those of the original whiskers (9.8 m^2/g and 0.03 cm^3/g).

Porous carbon films (C700, Figure 3a and b) were obtained after a 700 °C calcination on the pitch/whisker composite. The porous structure of the calcined whiskers has contributed to the formation of the porous carbon films. The carbonized pitch might have been activated by H_2O released from BMS whiskers during the calcination. With calcination at 900 °C, a hierarchically porous structure composing of carbon cages (labeled as C900) was obtained. The carbon cages have a cylindrical appearance similar to the BMS whiskers (Figure 3c), or a porous belt-like structure (Figure 3d) probably due to tearing of the porous cylinders. High resolution TEM (Figure 3e) and STEM observations (Figure 4) show that the carbon cages have three-dimensional pores in size of ∼20 nm and well-graphitized walls in thickness of 1−5 nm. Considering that the thermal decomposition of $MgSO_4$ starts at ∼900 °C (Supporting Information Figure S1), the carbon cages are

likely formed due to the etching of SO_x (x = 2 or 3) released by $MgSO_4$. Further increase of the calcination temperature to 1000 °C has produced a branch-like carbon material (labeled as C1000, Figure 3f), showing a corrupted porous structure due to the etching of excess SO_x. The yields of the S-doped carbons (the weight of carbon/the weight of pitch) are listed in Table 1.

Table 1. Characterization of the S-Doped Porous Carbons

samples	yield (wt %)	S content by XPS		S content by element analysis (wt %)	BET SSA (m²/g)	pore vol. (cm³/g)
		(at %)	(wt %)			
C700	49.2	10.1	22.5	26.8	658.6	0.85
C900	34.4	8.2	18.9	19.6	690.8	1.01
C1000	30.6	3.3	8.2	15.6	661.8	1.13

The yield decreases while the carbonization temperature increasing, indicating that more carbon atoms have been gasified due to the oxidization of SO_4^{2-} at higher temperature. The nitrogen adsorption isotherms and pore distributions of the S-doped carbons are shown in Figure 5, and the SSA values and pore volumes are summarized in Table 1. The BET SSAs of the S-doped carbons are in the range 650−700 m²/g. Two types of pores centralized at ∼3.8 and 17.5 nm are observed in the pore distribution curve of C900, well consistent with the hierarchically porous structure of C900 shown by the TEM observation.

EDS mapping (Figure 4) shows that S element is evenly distributed in C900. The Cu and Si peak in the EDS spectrum might come from the copper grid with carbon films. Usually, $MgSO_4$ is stable at 700 °C, and no decomposition of $MgSO_4$ is observed after a 700 °C calcination, as indicated by the XRD curve in Figure 6a. However, at the case for the BMS/asphalt composite, MgO peaks can be found in the XRD pattern of the material after a 700 °C calcination (Figure 6a). It means that $MgSO_4$ has decomposed at 700 °C with the existence of asphalt, thus providing S atoms for S doping. These results give a conclusive evidence showing that the S-doping reaction between $MgSO_4$ and asphalt, as shown in Figure 1b, has taken place at 700 °C. XPS analysis (Figure 6b) indicates an S concentration of 10.1 atom % for C700, 8.2 atom % for C900, and 3.3 atom % for C1000 (Table 1). The S concentration of 10.1 atom % (corresponding to 22.5 wt %) is higher than most reported S-doped carbon materials and close to the highest S doping level of up to 30 wt % (obtained by using $Na_2S_2O_3$ as S

source).[23,24] In previous reports, graphene oxide is often used as the starting material to prepare S-doped graphene via the reaction between oxygen-containing groups in GO and S-containing compounds[25] or pure S.[26] Recently, Liu et al.[23] reported the synthesis of S-doped carbons by moderating black powder chemistry with sulfate (K_2SO_4 and $Na_2S_2O_3$) as S source. In order to moderate the explosion, the reactants (sugar and sulfate) were diluted by chemically inert molten salt. Our results indicate that the sulfate anions (SO_4^{2-}) in $MgSO_4$ can mildly react with $-CH_x$ or C−C groups in asphalt to form C−S bonds, realizing S doping with a high S content. In the typical S 2p spectrum for the S-PCs (Figure 6c), the peaks at 164.3, 165.6, and 168.8 eV can be attributed to the S atoms with covalent bonds of S—C, S=C, and —SO_x (x = 2−4), respectively. About 87% S atoms are directly connected with carbon framework rather than existing in —SO_x groups. A control sample (labeled as G1) was prepared by a similar process but using porous MgO whiskers as templates (Supporting Information Figure S2), and no S element was detected in G1. Therefore, it is confirmed that the S doping at 700 °C is ascribed to the S-doping reaction between asphalt molecules and $MgSO_4$ (Figure 1b). N 1s peaks are observed in the XPS survey curves for all the porous carbons, with N concentrations in the range of 1.5−2.8 at%. The N atoms should origin from the N-containing compounds in pitch. The purity of C700 was also analyzed by ICP-AES. The content of Mg in the product is only 0.023 wt %, indicating that almost all MgO or Mg salts has been removed after acid washing.

In the high-resolution C 1s pattern of the pristine porous carbon G1 (Figure 6d), the peak at 284.8 eV corresponds to sp² carbon atoms, and the peaks at 285.9 and 288.7 eV are attributed to C—O and O—C=O bonding configurations.[27] Compared to G1, the S-doped porous carbon C700 (Figure 6e) has a higher content of sp² carbon atoms (71.0%) and a lower content of the O—C=O bonding configuration (4.2%). It indicates that the oxygen-containing groups have been reduced after the S doping reaction. TG analysis indicates that the thermal decomposition of $MgSO_4$ starts at ∼900 °C. With calcination at 900 or 1,000 °C, the SO_3 released by $MgSO_4$ thermal decomposition would preferentially react with the highly active S-doped structures, thus resulting in a lowered S content and more —SO_x groups (Supporting Information Figure S3). Considering the oxidizability of SO_4^{2-}, the removal of oxygen functional groups in C700 may be attributed to the oxidization of C=O into CO_2 or the S substitution of oxygen atoms during calcining with $MgSO_4$.
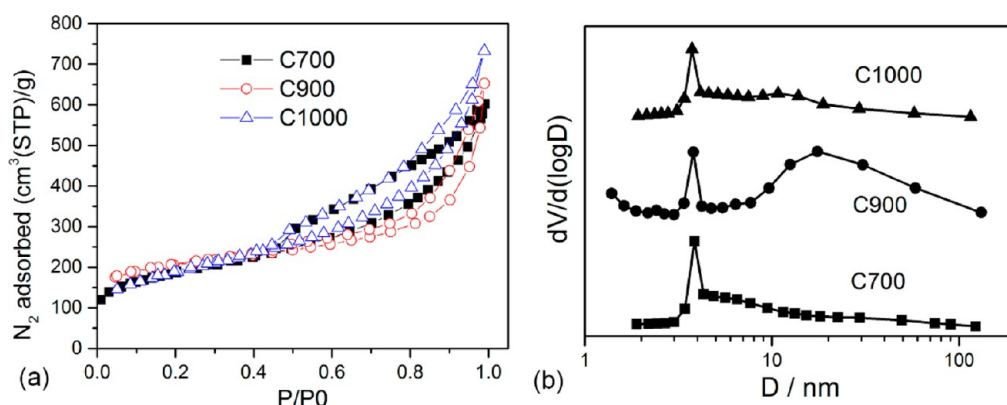

Figure 5. Nitrogen adsorption isotherms (a) and pore distributions (b) of the S-doped carbons.
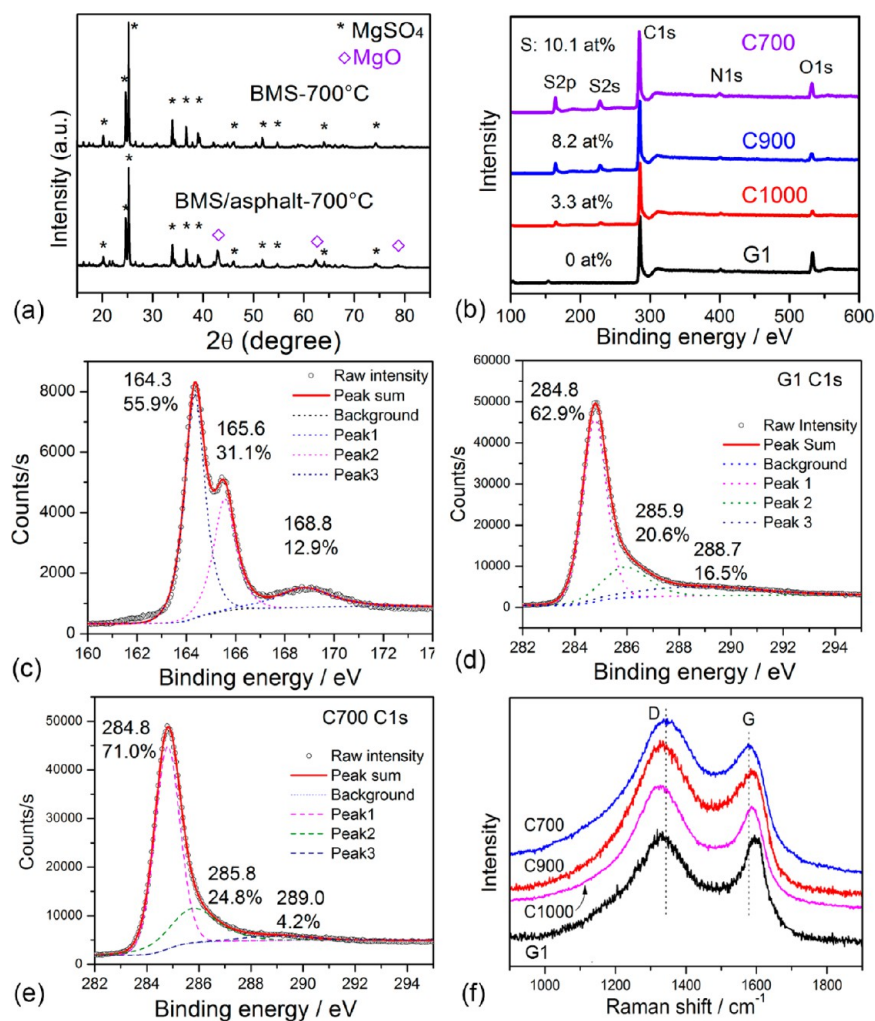
Figure 6. Characterization of the S-PCs. (a) XRD patterns of the 700 °C-calcined BMS whiskers and BMS/asphalt composite. (b) XPS survey data of the S-doped porous carbons in comparison with the undoped one G1. (c) XPS S 2p spectrum of C700. XPS C 1s spectra of G1 (d) and C700 (e). (f) Raman spectra of the S-doped porous carbons in comparison with the undoped porous carbon G1.

The S doping level in bulk was measured by elemental analysis. As listed in Table 1, the S content in bulk for C700 is as high as 26.8 wt %, indicating that the S doping process presented in this work is quite efficient to realize S doping with a high level. The S contents in bulk obtained by element analysis are obviously higher than the values in surface (3 nm in depth) obtained by XPS analysis. It indicates that the S-doped carbon segments in surface may be easily oxidized when contacting $MgSO_4$. The S content in surface for C1000 (8.2 wt %) is only 53% of that in bulk, showing that the oxidization by $MgSO_4$ is more severe at higher temperature (1000 °C).

Raman spectroscopy also provides direct proof for the S doping. In Figure 6f, obvious upshift in D bands and downshift in G bands are observed as the S content increasing, showing an important characteristic of n-type substitutional doping of carbon materials. An increase of the D to G ratios (I_D/I_G) is also observed after S doping, indicating that S-doping has aroused formation of more disorders in the carbon framework due to introduction of foreign atoms. The EDS mapping and XPS analysis coupled with Raman spectroscopy have strongly confirmed that S atoms have been successfully introduced into carbon frameworks via covalent bonds.

Figure 7a shows the current–voltage ($I–V$) curves of compressed pellets (the top left inset) containing a set amount

of porous carbons. Higher conductance is found at higher S content (the lower right inset of Figure 7a), indicating that the S doping has promoted the conductivity of the porous carbons. The graphitization degree, porosity, and morphology of G1 are similar to C700 because they were prepared with the same carbonization temperature of 700 °C. Therefore, the significantly enhanced electronic conductivity of C700, as compared to G1, should be attributed to the S doping rather than other factors. Yun et al.[26] have reported a similar promotion of the electrical conductivity in S-doped graphene nanosheets, showing that the conductivity of S-doped graphene nanosheets (1743 S m^{-1}) is 2 orders of magnitude higher than that of graphene nanosheets (32 S m^{-1}). Our results is also well consistent with the theoretical calculation on S-doped graphene, which can exhibit better metallic properties than the pristine graphene sheet at a S concentration ~4 at %.[28] The structural distortions caused by the S atoms increase the metallic properties of graphene, which might explain why the conductivity has been enhanced by S doping for the porous carbon. The enhanced electronical conductivity aroused by S doping is in favor of improving the rate capability because of the quick charge transfer.

Electrochemical tests were performed via assembling coin-type cells using the as-prepared porous carbons as anode
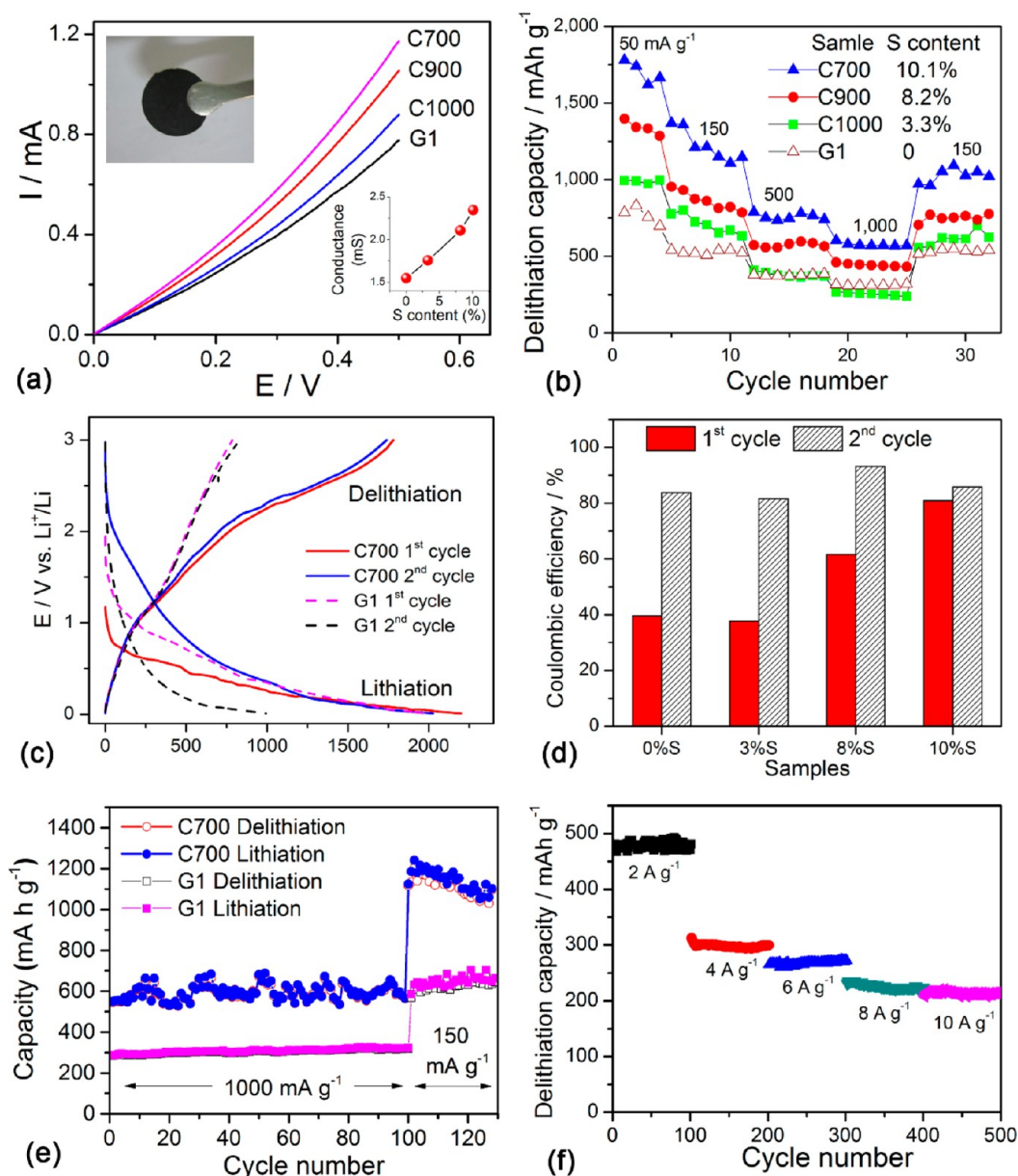
Figure 7. Electrochemical properties of the S-PCs. (a) Conductivity of porous carbons with different S concentrations. (b) Rate capabilities of the S-PCs in comparison with the undoped porous carbons. (c) Typical lithiation−delithiation curves of the S-doped carbon cages for the 1st and 2nd cycles at the constant current of 50 mA g^{-1}. (d) Coulombic efficiencies of the carbon materials with different S contents for the 1st and 2nd cycles at 50 mA g^{-1}. (e) Cycling performance of the S-doped (C700) and the undoped (G1) porous carbons. (f) High rate cycling performance of C700.

materials. As shown in Figure 7b, higher delithiation capacity is obtained at higher S content, indicating that S-doped carbon segments have larger Li storage capacity than pure carbon.[13,26] The highest capacity (1781 mA h g^{-1} at the current density of 50 mA g^{-1}) is obtained at the S content of 10.1 atom %, which is more than two times that of the undoped porous carbon (832 mA h g^{-1} at 50 mA g^{-1}). The reversible capacity delivered by C700 (1781 mA h g^{-1} at 50 mA g^{-1}) is obviously higher than the capacity delivered by S-doped porous carbons hybridized with graphene (1400 mA h g^{-1} at 50 mA g^{-1}) reported by Yan et al.[29] The Li storage capacity at 1000 mA g^{-1} for C700 reaches 604 mA h g^{-1}, showing excellent rate capability.

Figure 7c shows typical lithiation−delithiation curves of C700 in comparison with G1. The lithiation and delithiation capacities of C700 at the current density of 50 mA g^{-1} are 2200

and 1781 mA h g^{-1}, respectively, in the first cycle. The reversible lithiation capacity between 0.5 and 0 V for C700 is 1244 mA h g^{-1} in the second cycle. It is noticeable that the Coulombic efficiency in the first cycle for C700 (81.0%) is much higher than that for G1 (39.6%). As shown in Figure 7d, higher Coulombic efficiencies in the first cycles, corresponding to less irreversible Li storage, are obtained at higher S contents, indicating that S doping has contributed to reducing the irreversible Li storage capacity. The initial Coulombic efficiency of C700 (81.0%) is superior as compared to the recently reported graphene-based materials (e.g., 51% for S-doped graphene sheets,[26] 68% for NiO nanosheet/graphene composite,[30] and 56% for S-doped porous carbons hybridized with graphene[29]).

Cycling performance of the porous carbons is shown in Figure 7e and f. Almost no capacity decay is observed for both
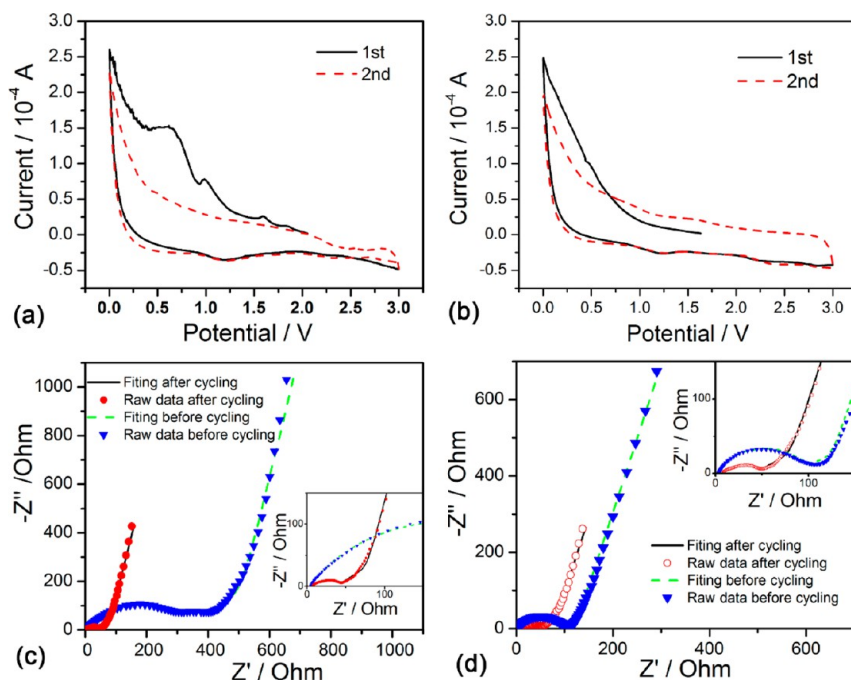
Figure 8. CV curves of G1 (a) and C700 (b). AC impedance curves of G1 (c) and C700 (d). The insets of c and d are the magnified impedance curves.
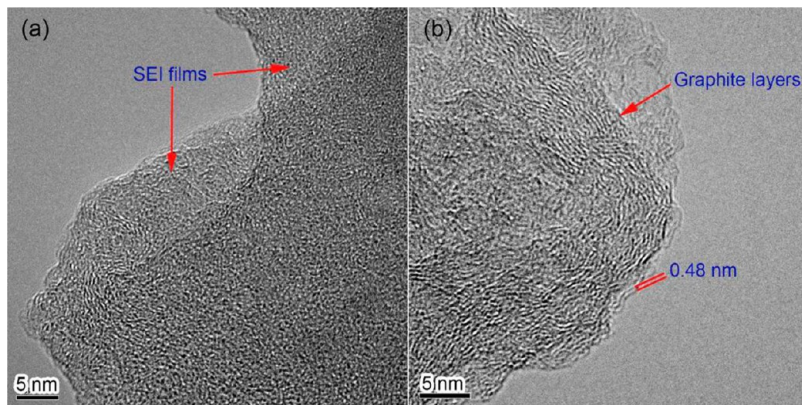

Figure 9. Porous carbons after electrochemical tests. High resolution TEM images of the undoped (a, G1) and the S-doped (b, C700) porous carbons after 30 charge−discharge cycles.

G1 and C700 after 100 cycles at 1000 mA g^{-1}. At the current density of 150 mA g^{-1}, a capacity of 1096 mA h g^{-1} is obtained for C700 after 130 cycles, which is much higher than that for G1 (647 mA h g^{-1}). Figure 7f shows that the S-PCs exhibit excellent cycling stability at high rate. A specific capacity of 214 mA h g^{-1} is retained at the current density of 10 A g^{-1} after even 500 cycles, showing better rate capability as compared to the hierarchically porous carbon monoliths reported by Hu et al. (150 mA h g^{-1} at ~11 A g^{-1}).[4] The excellent rate capability can be attributed to the enhanced conductivity, the larger Li storage capacity of S-doped carbon segments and the porous structure of the S-PCs, which are propitious to the quick charge transfer and the fast diffusion of Li ions by reducing the diffusion distance.[14,15] In addition, although the as-prepared porous carbons are also doped by N atoms, the contribution from N doping is quite limited as considering the fact that C900 and C1000 have lower N doping but exhibit higher Li storage capacity as compared to G1 (Supporting Information Figure S4).

The enhanced Coulombic efficiency is partially explained in Figure 8a and b, which compare the cyclic voltammetry (CV) curves of the S-PC (C700) and the undoped porous carbon (G1). In the CV pattern of the undoped porous carbon, a cathodic peak in the first cycle is observed at 0.7 V, corresponding to the irreversible Li$^+$ consumption due to formation of SEI films on the surface of the anode. Such a cathodic peak disappears in the CV pattern of the S-PC, indicating that the formation of SEI films on carbon surfaces is obviously affected by the S-doping. AC impedance curves of G1 and C700 are shown in Figure 8c and d. The equivalent circuit shown in Supporting Information Figure S5 was used to fit the impedance data for the electrodes before and after charge−discharge cycling. The SEI film resistance (R_f) and the charge-transfer resistance (R_{ct}) are obviously reduced after the charge−discharge test as compared to those before cycling, indicating that much better contact between electrolyte and electrode materials has been realized after the cycling. After the rate test, the SEI film resistance (R_f) for C700 (14.5 Ω) is smaller than
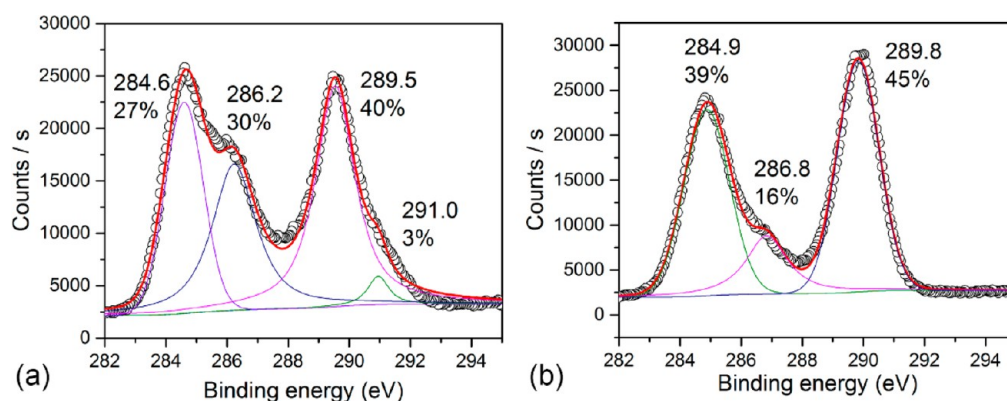
Figure 10. C 1s XPS spectra of the undoped porous carbon G1 (a) and the S-doped porous carbon C700 (b) after charge−discharge cycling. The scattered open circles present raw data, and the lines correspond to multipeak fitting results.

that for G1 (20.3 Ω), indicating that thinner SEI films have been formed on C700. Figure 9 shows the TEM images of the two carbon materials after 30 charge−discharge cycles. No clear dark lines corresponding to graphite layers are found on the surface of the undoped porous carbon (Figure 9a), indicating that thick SEI films have been formed. In contrast, clear graphite layers without thick SEI films are observed on the edges of the S-PC (Figure 9b), well consistent with the analysis of the CV patterns.

XPS C 1s spectra of G1 and C700 after charge−discharge cycling are shown in Figure 10. The peaks at 284.6−284.9 eV can be attributed to graphitic carbon atoms with C=C bonds (as shown in Figure 6d and e). The peaks at 286.2−286.8 eV observed for both the two samples should correspond to C−O and C=O bonds.[27] The strong peaks at 289.5 for G1 and 289.8 eV for C700 should be attributed to the C atoms in LiCO$_3$. In the C 1s spectrum of G1 after cycling, the small peak at 291.0 eV can be attributed to C−CO$_3$ or CF$_2$ bonds. Compared to C700, the peak corresponding to C−O and C=O bonds for G1 (286.2 eV) is much stronger. If the C atoms in LiCO$_3$ are excluded, 53% of the carbon atoms in the SEI films of G1 exist in oxygen-containing groups, much higher than the percentage in the SEI films on C700 (29%). This might be the reason why clear graphite layers without thick SEI films are observed on the edges of C700 after charge−discharge cycling (Figure 9).

The suggested mechanism for the enhancement of the Coulombic efficiency aroused by S doping is illustrated in Figure 11. Irreversible Li storage is usually aroused by the irreversible lithium combination with oxygen-containing functional groups (C=O, C−OH) or active carbon atoms (C*), which leads to the formation of SEI films on carbon

surfaces.[2,31,32] The main components of the SEI films are Li$_2$CO$_3$, ROCO$_2$Li, etc., corresponding to the irreversible combination of Li ions. Prelithiation[33] or Co$_3$O$_4$ saturation[20] of the active sites has been demonstrated to be capable of reducing irreversible Li storage and enhancing Coulombic efficiency. However, selective removal of these active sites has not been reported. As shown in Figure 11, the O-containing functional groups or active carbon atoms that contribute to the irreversible Li storage might have been removed in the S-doping reaction due to oxidation of SO$_x$ or S substitution, thus resulting in a promoted Coulombic efficiency. Our results indicate that the Li storage in S-doped carbon segments is well reversible.

4. CONCLUSIONS

In summary, S-PCs with S doping up to 10.1 atom % have been produced by carbonization of pitch using BMS whiskers as both S source and templates. EDS mapping and XPS analysis companied with Raman spectra have confirmed that the S atoms are evenly introduced into carbon frameworks via covalent bonds. Compared to the undoped porous carbon, the S-PCs exhibit significantly enhanced Li storage capacity, Coulombic efficiency, and high rate capability, with an excellent cycling stability. The significant promotion of the Coulombic efficiency in the first cycle can be attributed to the selective removal of active carbon atoms that tend to irreversibly combine with Li ions during the S doping reaction. Our work demonstrates a scalable synthesis of S-PCs, and provides a reliable new strategy to promote the electrode performance by S-doping.

■ ASSOCIATED CONTENT

Ⓢ Supporting Information

TG curves of the BMS whiskers, electron microscopy observation of the porous MgO whiskers and G1, S 2p spectra and N contents for the porous carbons, and the equivalent circuit used to fit the impedance data. This material is available free of charge via the Internet at http://pubs.acs.org/.

■ AUTHOR INFORMATION

Corresponding Author

*Tel.: 8610-89733085, Email: ngq@cup.edu.cn.

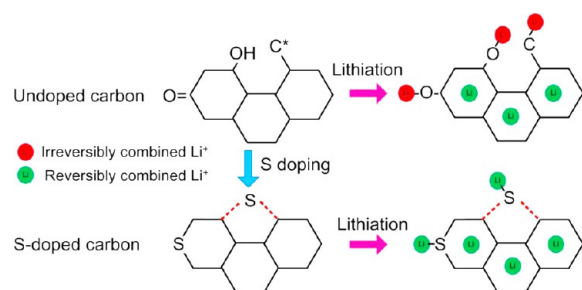### Author Contributions

§G.N. and X.M. contributed equally.

Figure 11. Suggested mechanism for enhancing the initial Coulombic efficiency by S doping.

■ REFERENCES

(1) Luo, B.; Liu, S.; Zhi, L. Chemical Approaches toward Graphene-Based Nanomaterials and Their Applications in Energy-Related Areas. *Small* **2012**, *8*, 630−646.

(2) Kaskhedikar, N. A.; Maier, J. Lithium Storage in Carbon Nanostructures. *Adv. Mater.* **2009**, *21*, 2664−2680.

(3) Yang, S.; Feng, X.; Zhi, L.; Cao, Q.; Maier, J.; Mullen, K. Nanographene-Constructed Hollow Carbon Spheres and Their Favorable Electroactivity with Respect to Lithium Storage. *Adv. Mater.* **2010**, *22*, 838−42.

(4) Hu, Y. S.; Adelhelm, P.; Smarsly, B. M.; Hore, S.; Antonietti, M.; Maier, J. Synthesis of Hierarchically Porous Carbon Monoliths with Highly Ordered Microstructure and Their Application in Rechargeable Lithium Batteries with High-Rate Capability. *Adv. Funct. Mater.* **2007**, *17*, 1873−1878.

(5) Pan, D.; Wang, S.; Zhao, B.; Wu, M.; Zhang, H.; Wang, Y.; Jiao, Z. Li Storage Properties of Disordered Graphene Nanosheets. *Chem. Mater.* **2009**, *21*, 3136−3142.

(6) Guo, P.; Song, H. H.; Chen, X. H. Electrochemical Performance of Graphene Nanosheets as Anode Material for Lithium-Ion Batteries. *Electrochem. Commun.* **2009**, *11*, 1320−1324.

(7) Tang, K.; White, R. J.; Mu, X.; Titirici, M.-M.; van Aken, P. A.; Maier, J. Hollow Carbon Nanospheres with a High Rate Capability for Lithium-Based Batteries. *ChemSusChem* **2012**, *5*, 400−403.

(8) Zhou, X.; Guo, Y.-G. Highly Disordered Carbon as a Superior Anode Material for Room-Temperature Sodium-Ion Batteries. *ChemElectroChem.* **2014**, *1*, 83−86.

(9) Panchakarla, L. S.; Govindaraj, A.; Rao, C. N. R. Boron- and Nitrogen-Doped Carbon Nanotubes and Graphene. *Inorg. Chim. Acta* **2010**, *363*, 4163−4174.

(10) Wang, H.; Zhang, C.; Liu, Z.; Wang, L.; Han, P.; Xu, H.; Zhang, K.; Dong, S.; Yao, J.; Cui, G. Nitrogen-Doped Graphene Nanosheets with Excellent Lithium Storage Properties. *J. Mater. Chem.* **2011**, *21*, 5430−5434.

(11) Reddy, A. L. M.; Srivastava, A.; Gowda, S. R.; Gullapalli, H.; Dubey, M.; Ajayan, P. M. Synthesis of Nitrogen-Doped Graphene Films for Lithium Battery Application. *ACS Nano* **2010**, *4*, 6337−6342.

(12) Shin, W. H.; Jeong, H. M.; Kim, B. G.; Kang, J. K.; Choi, J. W. Nitrogen-Doped Multiwall Carbon Nanotubes for Lithium Storage with Extremely High Capacity. *Nano Lett.* **2012**, *12*, 2283−8.

(13) Liu, J.; Li, X.; Yang, J.; Geng, D.; Li, Y.; Wang, D.; Li, R.; Sun, X.; Cai, M.; Verbrugge, M. W. Microwave-Assisted Hydrothermal Synthesis of Nanostructured Spinel $Li_4Ti_5O_{12}$ as Anode Materials for Lithium Ion Batteries. *Electrochim. Acta* **2012**, *63*, 100−104.

(14) Fan, Z.; Yan, J.; Ning, G.; Wei, T.; Zhi, L.; Wei, F. Porous Graphene Networks as High Performance Anode Materials for Lithium Ion Batteries. *Carbon* **2013**, *60*, 558−561.

(15) Fang, Y.; Lv, Y.; Che, R.; Wu, H.; Zhang, X.; Gu, D.; Zheng, G.; Zhao, D. Two-Dimensional Mesoporous Carbon Nanosheets and Their Derived Graphene Nanosheets: Synthesis and Efficient Lithium Ion Storage. *J. Am. Chem. Soc.* **2013**, *135*, 1524−1530.

(16) Yoo, E. J.; Kim, J.; Hosono, E.; Zhou, H.; Kudo, T.; Honma, I. Large Reversible Li Storage of Graphene Nanosheet Families for Use in Rechargeable Lithium Ion Batteries. *Nano Lett.* **2008**, *8*, 2277−2282.

(17) Lian, P.; Zhu, X.; Liang, S.; Li, Z.; Yang, W.; Wang, H. Large Reversible Capacity of High Quality Graphene Sheets as an Anode Material for Lithium-Ion Batteries. *Electrochim. Acta* **2010**, *55*, 3909−3914.

(18) Goodenough, J. B.; Kim, Y. Challenges for Rechargeable Li Batteries. *Chem. Mater.* **2010**, *22*, 587−603.

(19) Ma, H.; Cheng, F.; Chen, J. Y.; Zhao, J. Z.; Li, C. S.; Tao, Z. L.; Liang, J. Nest-Like Silicon Nanospheres for High-Capacity Lithium Storage. *Adv. Mater.* **2007**, *19*, 4067−4070.

(20) Zhu, X.; Ning, G.; Ma, X.; Fan, Z.; Xu, C.; Gao, J.; Xu, C.; Wei, F. High Density Co_3O_4 Nanoparticles Confined in a Porous Graphene Nanomesh Network Driven by an Electrochemical Process: Ultra-High Capacity and Rate Performance for Lithium Ion Batteries. *J. Mater. Chem. A* **2013**, *1*, 14023−14030.

(21) Liu, F.; Xiang, L.; Jin, Y. Hydrothermal Synthesis Process of Magnesium Oxysulfate Whiskers. *J. Inorg. Mater.* **2004**, *19*, 784−788.

(22) Sun, X. T.; Shi, W. T.; Xiang, L.; Zhu, W. C. Controllable Synthesis of Magnesium Oxysulfate Nanowires with Different Morphologies. *Nanoscale Res. Lett.* **2008**, *3*, 386−389.

(23) Liu, X.; Antonietti, M. Moderating Black Powder Chemistry for the Synthesis of Doped and Highly Porous Graphene Nanoplatelets and Their Use in Electrocatalysis. *Adv. Mater.* **2013**, *25*, 6284−6290.

(24) Kiciński, W.; Szala, M.; Bystrzejewski, M. Sulfur-Doped Porous Carbons: Synthesis and Applications. *Carbon* **2014**, *68*, 1−32.

(25) Yang, Z.; Yao, Z.; Li, G.; Fang, G.; Nie, H.; Liu, Z.; Zhou, X.; Chen, X. a.; Huang, S. Sulfur-Doped Graphene as an Efficient Metal-Free Cathode Catalyst for Oxygen Reduction. *ACS Nano* **2012**, *6*, 205−211.

(26) Yun, Y. S.; Le, V.-D.; Kim, H.; Chang, S.-J.; Baek, S. J.; Park, S.; Kim, B. H.; Kim, Y.-H.; Kang, K.; Jin, H.-J. Effects of Sulfur Doping on Graphene-Based Nanosheets for Use as Anode Materials in Lithium-Ion Batteries. *J. Power Sources* **2014**, *262*, 79−85.

(27) Sheng, Z. H.; Shao, L.; Chen, J. J.; Bao, W. J.; Wang, F. B.; Xia, X. H. Catalyst-Free Synthesis of Nitrogen-Doped Graphene Via Thermal Annealing Graphite Oxide with Melamine and Its Excellent Electrocatalysis. *ACS Nano* **2011**, *5*, 4350−8.

(28) Denis, P. A.; Faccio, R.; Mombru, A. W. Is It Possible to Dope Single-Walled Carbon Nanotubes and Graphene with Sulfur? *ChemPhysChem* **2009**, *10*, 715−722.

(29) Yan, Y.; Yin, Y.-X.; Xin, S.; Guo, Y.-G.; Wan, L.-J. Ionothermal Synthesis of Sulfur-Doped Porous Carbons Hybridized with Graphene as Superior Anode Materials for Lithium-Ion Batteries. *Chem. Commun.* **2012**, *48*, 10663−10665.

(30) Zhou, G.; Wang, D.-W.; Yin, L.-C.; Li, N.; Li, F.; Cheng, H.-M. Oxygen Bridges between Nio Nanosheets and Graphene for Improvement of Lithium Storage. *ACS Nano* **2012**, *6*, 3214−3223.

(31) Sun, Y.; Wu, Q.; Shi, G. Graphene Based New Energy Materials. *Energy Environ. Sci.* **2011**, *4*, 1113−1132.

(32) Béguin, F.; Chevallier, F.; Vix-Guterl, C.; Saadallah, S.; Bertagna, V.; Rouzaud, J. N.; Frackowiak, E. Correlation of the Irreversible Lithium Capacity with the Active Surface Area of Modified Carbons. *Carbon* **2005**, *43*, 2160−2167.

(33) Hassoun, J.; Lee, K. S.; Sun, Y. K.; Scrosati, B. An Advanced Lithium Ion Battery Based on High Performance Electrode Materials. *J. Am. Chem. Soc.* **2011**, *133*, 3139−43.